Excited state nucleon spectrum with two flavors of dynamical fermions

John M. Bulava,[1,*] Robert G. Edwards,[2,†] Eric Engelson,[3,‡] Justin Foley,[1,§] Bálint Joó,[2,‖] Adam Lichtl,[4,¶]
Huey-Wen Lin,[2,**] Nilmani Mathur,[5,††] Colin Morningstar,[1,‡‡] David G. Richards,[2,§§] and Stephen J. Wallace[3,‖‖]

[1]*Department of Physics, Carnegie Mellon University, Pittsburgh, Pennsylvania 15213, USA*
[2]*Thomas Jefferson National Accelerator Facility, Newport News, Virginia 23606, USA*
[3]*Department of Physics, University of Maryland, College Park, Maryland 20742, USA*
[4]*RIKEN-BNL Research Center, Brookhaven National Laboratory, Upton, New York 11973, USA*
[5]*Department of Theoretical Physics, Tata Institute of Fundamental Research, Mumbai 400005, India*
(Received 30 December 2008; published 23 February 2009)

Highly excited states for isospin $\frac{1}{2}$ baryons are calculated for the first time using lattice QCD with two flavors of dynamical quarks. Anisotropic lattices are used with two pion masses, $m_\pi = 416(36)$ MeV and 578(29) MeV. The lowest four energies are reported in each of the six irreducible representations of the octahedral group at each pion mass. The lattices used have dimensions $24^3 \times 64$, spatial lattice spacing $a_s \approx 0.11$ fm, and temporal lattice spacing $a_t = \frac{1}{3} a_s$. Clear evidence is found for a $\frac{5}{2}^-$ state in the pattern of negative-parity excited states. This agrees with the pattern of physical states and spin $\frac{5}{2}$ has been realized for the first time on the lattice.

I. INTRODUCTION

A major goal for lattice quantum chromodynamics (QCD) is the determination of the spectrum of the excited states of QCD. This goal is a complement to experimental work that studies the hadrons and their excitations and decays. In recent years, large amounts of data have been collected at Jefferson Laboratory regarding the spectrum of excitations of nucleons. The Excited Baryon Analysis Center aims to analyze the data using the best hadronic models available [1,2]. Lattice QCD calculations are needed as a means to link this program to the Lagrangian of QCD.

When QCD was formulated as the basic theory that would explain hadrons and their excited states, it could not be solved for the mass spectrum from first principles because of its nonperturbative nature. Much effort over the past 30 years has been devoted to developing the methods and tools to solve QCD on a lattice. Accurate resolution of the excited states of hadrons using lattice QCD has proven difficult. In Euclidean space, excited-state correlation functions decay faster than the ground state. At large times, the signals for excited states are swamped by the signals for lower energy states. Improved resolution in the temporal direction is essential for progress. An anisotropic lattice

where the temporal lattice spacing is finer than spatial spacings can provide better resolution while avoiding the increase in computational cost associated with a similar reduction of all spacings. The improved resolution must be combined with two other ingredients. A large number of operators is required that overlap well with excited states. The use of variational methods is essential to separate the excited states.

Large sets of baryon operators were developed and projected to the irreducible representations of the octahedral group in Refs. [3,4]. Link smearing and quark smearing were found to both be needed in order to optimize the quality of the signals that are obtained with the operators in Ref. [5]. Variational methods were used to determine the spectra of $I = \frac{1}{2}$ and $I = \frac{3}{2}$ excited baryons using the quenched approximation in Ref. [6].

In this work, we take another step toward the goal of determining the spectrum of nucleon excited states by studying the spectrum of isospin $\frac{1}{2}$ excited baryons in two-flavor QCD, using u and d quarks that have the same mass. Results are obtained on $24^3 \times 64$ lattices with two values of the pion mass: 416(36) MeV and 578 (29) MeV.

In the physical spectrum for isospin $\frac{1}{2}$ the lowest three states are the nucleon, N, the Roper resonance, N' (P_{11}), and the opposite-parity N^* (S_{11}). Quenched lattice QCD calculations [7–12] generally have found a spectrum inverted with respect to experiment, with the N' heavier than the negative-parity N^*. An exception is the calculation of the Kentucky group [13] that obtained the correct mass ordering with a pion mass below 400 MeV (after subtracting the effects of the quenched "ghosts"). This has helped to motivate full-QCD simulations where the spectrum can be determined without unphysical contributions from ghost states. Moreover, many additional excited states have been

*jbulava@andrew.cmu.edu
†edwards@jlab.org
‡engelson@umd.edu
§jfoley@andrew.cmu.edu
‖bjoo@jlab.org
¶alichtl@bnl.gov
**hwlin@jlab.org
††nilmani@theory.tifr.res.in
‡‡colin_morningstar@cmu.edu
§§dgr@jlab.org
‖‖stevewal@umd.edu

observed experimentally that should be reproduced by lattice QCD and full-QCD simulations are needed as a complement to the experimental searches for new excited states.

Anisotropic techniques have been adopted in lattice calculations for relativistic heavy-quark actions for the spectrum of charmonium [14,15], for calculations of the spectrum of glueballs [16], and to extract excited baryon states [3,4,6,17–20]. Previous results using anisotropic lattices include two-flavor anisotropic dynamical simulations performed by CP-PACS [21] and the TrinLat Collaborations [22].

In this work, we report the nucleon spectrum using the interpolating basis from Refs. [3,4] on two-flavor, anisotropic, Wilson fermion and Wilson gauge configurations. The action parameters and bare gauge and fermion anisotropies are tuned such that the gauge anisotropy (as determined from Wilson-loop ratios) and the fermion anisotropy (as determined from the meson dispersion relation) are both consistent with the desired renormalized anisotropy $a_s/a_t = 3$. Our configurations were generated using the CHROMA [23] hybrid Monte Carlo (HMC) code with multi-time-scale integration.

The organization of this paper is as follows: In Sec. II, we discuss the details of the actions used and their parameters. Then in Sec. III we discuss the HMC used in this work and show how it is applied to anisotropic lattices with mass preconditioning. Section IV presents results for the conventional determination of hadron masses and the anisotropy from two-point correlation functions and Sec. V presents our procedure and results for setting the lattice scale in physical units. Section VI discusses the construction of large numbers of baryon operators in the relevant irreducible representations of the octahedral group and demonstrates the noise suppression that is obtained by smearing both the quark and gauge fields. Section VII presents results for the $I = \frac{1}{2}$ baryon spectrum for pion masses of 416 and 578 MeV using $N_f = 2$ lattices. Clear evidence for a spin $\frac{5}{2}^-$ state is presented. Some conclusions are presented in Sec. VIII.

II. LATTICE ACTIONS

In this section, we describe the gauge and fermion actions used in this calculation. For the gauge sector, we use a Wilson anisotropic gauge action

$$S_G^\xi[U] = \frac{\beta}{N_c \xi_0} \left\{ \sum_{x,s \neq s'} \Omega_{\mathcal{P}_{ss'}}(x) + \sum_{x,s} \xi_0^2 \Omega_{\mathcal{P}_{st}}(x) \right\}, \quad (1)$$

where $\Omega_W = \operatorname{Re} \operatorname{Tr}(1 - \mathcal{P})$ and $\mathcal{P}$ is the plaquette

$$\mathcal{P}_{\mu\nu}(x) = U_\mu(x) U_\nu(x+\mu) U_\mu^\dagger(x+\nu) U_\nu^\dagger(x). \quad (2)$$

The coupling g^2 appears in $\beta = 2N_c/g^2$. The parameter ξ_0 is the bare gauge anisotropy. In the fermion sector, we adopt the anisotropic Wilson fermion action [24]

$$S_F^\xi[U, \bar{\psi}, \psi] = a_s^3 a_t \sum_x \bar{\psi}(x) M_W \psi(x),$$

$$M_W = m_0 + \nu_t \mathcal{W}_t + \nu_s \mathcal{W}_s, \quad (3)$$

where

$$\mathcal{W}_\mu = \nabla_\mu - \frac{a_\mu}{2} \gamma_\mu \Delta_\mu,$$

$$\nabla_\mu f(x) = \frac{1}{2a_\mu} [U_\mu(x) f(x+\mu) - U_\mu^\dagger(x-\mu) f(x-\mu)],$$

$$\Delta_\mu f(x) = \frac{1}{a_\mu^2} [U_\mu(x) f(x+\mu)$$
$$+ U_\mu^\dagger(x-\mu) f(x-\mu) - 2f(x)]. \quad (4)$$

In terms of dimensionless variables $\hat{\psi} = a_s^{3/2} \psi$, $\hat{m}_0 = m_0 a_t$, $\hat{\nabla}_\mu = a_\mu \nabla_\mu$, $\hat{\Delta}_\mu = a_\mu^2 \Delta_\mu$, and the dimensionless "Wilson operator" $\hat{\mathcal{W}}_\mu \equiv \hat{\nabla}_\mu - \frac{1}{2} \gamma_\mu \hat{\Delta}_\mu$, we find that the fermion matrix M_W becomes

$$M_W = \frac{1}{a_t} \left\{ a_t \hat{m}_0 + \nu_t \hat{\mathcal{W}}_t + \frac{\nu_s}{\xi_0} \sum_s \hat{\mathcal{W}}_s \right\}. \quad (5)$$

Because it is possible to redefine the fields as in Refs. [25,26], one coefficient (either ν_t or ν_s) is redundant; here we set $\nu_t = 1$ and $\nu_s = \nu$ for tuning. For convenience of parametrization, we use the bare gauge and fermion anisotropies, $\gamma_{g,f}$, defined as

$$\gamma_g = \xi_0, \qquad \gamma_f = \frac{\xi_0}{\nu}. \quad (6)$$

The parameters γ_g, γ_f and the quark mass m_0 require tuning in order to realize the desired renormalization constraints. The bare gauge and fermion anisotropy parameters γ_g and γ_f are tuned to obtain the desired renormalized gauge and fermion anisotropies (ξ_g and ξ_f): both equal to $a_s/a_t = 3.0$. The renormalized gauge anisotropy (ξ_g) can be determined from the static-quark potential using Klassen's "Wilson-loop ratio" [27]:

$$R_{ss}(x, y) = \frac{W_{ss}(x, y)}{W_{ss}(x+1, y)} \xrightarrow{\text{asym}} e^{-a_s V_s(y a_s)},$$
$$R_{st}(x, t) = \frac{W_{st}(x, t)}{W_{st}(x+1, t)} \xrightarrow{\text{asym}} e^{-a_s V_s(t a_t)}, \quad (7)$$

where W_{st} are the Wilson loops involving the temporal direction, and W_{ss} are those involving only the spatial directions. We determine the renormalized gauge anisotropy ξ_g by minimizing [21]

$$L(\xi_g) = \sum_{x,y} \frac{(R_{ss}(x, y) - R_{st}(x, \xi_g y))^2}{(\Delta R_s)^2 + (\Delta R_t)^2}, \quad (8)$$

where ΔR_s and ΔR_t are the statistical errors of R_{ss} and R_{st}. A fixed background gauge field in the spatial z direction is used following the Schrödinger-functional scheme [28]

which allows for a determination of the critical mass using the partially conserved axial-vector current Ward identity. For more details, see Sec. IV B of Ref. [29]. We determine the renormalized fermion anisotropy ξ_f through the conventional relativistic meson dispersion relation as will be discussed in Sec. IVA.

We find that when $\xi_g = \xi_0 = 2.38$, $\nu = 1$ (or $\xi_f = \xi_0 = 2.38$), ξ_g and ξ_f (see Sec. IVA) are consistent with 3, given our other choices of parameters. The critical mass at these bare parameters is $m_c = -0.41473$. The m_0 parameter within our range of interest has negligible effect on the anisotropies. (Similar results are observed in the three-flavor anisotropic clover action study in Ref. [29].) We set m_0 to -0.4086 and -0.4125 for our pion-mass study.

III. ALGORITHM

The anisotropic Wilson configurations were generated with the HMC algorithm [30]. To increase the efficiency of the method we employed several techniques such as Hasenbusch style mass preconditioning [31], the use of multiple time-scale integration schemes [32], chronological inversion methods [33] during the molecular dynamics, and evolving the temporal links with different time steps than the spatial ones [22]. We discuss some of the pertinent details next.

A. Hybrid Monte Carlo

The basic technique for gauge generation is a Markov chain Monte Carlo method where one moves from an initial gauge configuration to a successive one by generating a new trial configuration and then performing an acceptance/rejection test upon the new one. If the trial configuration is accepted, it becomes the next configuration in the chain, otherwise the original configuration becomes the next state in the chain.

In order to use a global Metropolis accept/reject step with a reasonable acceptance rate, the space of states is extended to include momenta $\pi_\mu(x)$ canonical to the gauge links $U_\mu(x)$ so that one may define a Hamiltonian

$$H = \frac{1}{2}\sum_{x,\mu} \pi_\mu(x)^\dagger \pi_\mu(x) + S(U), \qquad (9)$$

where S is the action. It is then possible to propose new configurations from previous ones by performing Hamiltonian molecular dynamics (MD) to get from the initial to the proposed state. Using a reversible and area-preserving MD evolution maintains detailed balance, which is sufficient for the algorithm to converge. In order to ensure ergodicity in the entire phase space, the momenta need to change periodically. This can be accomplished by refreshing the momenta from a Gaussian heat bath prior to the MD update step.

In order to deal with the fermion determinant, it is standard to use the method of pseudofermions. One inte-

grates out the Grassman-valued fermion fields in the action and rewrites the resulting determinant as an integral over bosonic fields,

$$Z = \int [d\bar{\eta}][d\eta]e^{-\bar{\eta}\mathcal{D}\eta} = \det(\mathcal{D})$$

$$= \int [d\phi^\dagger][d\phi]e^{-\phi^\dagger\mathcal{D}^{-1}\phi}, \qquad (10)$$

where η and $\bar{\eta}$ are the Grassman-valued fields, $\mathcal{D}$ is some Hermitian, positive-definite kernel, and $\phi^\dagger$ and ϕ are the bosonic pseudofermion fields. Our phase space is thus enlarged to include also the pseudofermion fields. Similar to the momenta, these fields need to be refreshed before each MD step to carry out the pseudofermion integral.

In the case of a two-flavor simulation, $\mathcal{D}$ is typically of the form,

$$\mathcal{D} = Q^\dagger Q. \qquad (11)$$

For the rest of this work Q is an even-odd preconditioned fermion matrix for an individual flavor of fermion. In this case $\mathcal{D}$ is manifestly Hermitian and positive definite, and the integral in Eq. (10) is guaranteed to exist. Furthermore, the pseudofermion fields can easily be refreshed by producing a vector χ filled with Gaussian noise with a variance of $\frac{1}{2}$ and then forming $\phi = Q^\dagger \chi$.

B. Multiple time-scale anisotropic molecular dynamics update

While any reversible and area-preserving MD update scheme can be used in the MD step, the acceptance rate is controlled by the truncation error in the scheme. This manifests itself as a change in the Hamiltonian, δH, over an MD trajectory, since we use the Metropolis acceptance probability

$$P_{\text{acc}} = \min(1, e^{-\delta H}). \qquad (12)$$

We may easily construct a reversible scheme by combining symplectic update steps $\mathcal{U}_p(\delta\tau)$ and $\mathcal{U}_q(\delta\tau)$ which update momenta and coordinates by a time step of length $\delta\tau$, respectively,

$$\mathcal{U}_p(\delta\tau_\mu): (\pi_\mu(x), U_\mu(x)) \rightarrow (\pi_\mu(x) + F_\mu(x)\delta\tau_\mu, U_\mu(x)), \qquad (13)$$

$$\mathcal{U}_q(\delta\tau_\mu): (\pi_\mu(x), U_\mu(x)) \rightarrow (\pi_\mu(x), e^{i\pi_\mu\delta\tau_\mu}U_\mu(x)), \qquad (14)$$

where $F_\mu(x)$ is the MD force coming from the variation of the action with respect to the gauge fields. We emphasize that one may update all the links pointing in direction μ with a separate step size $\delta\tau_\mu$. While this may not be useful in isotropic simulations, in an anisotropic calculation with one fine direction, it may be advantageous to use a shorter

time step to update the links in that direction to ameliorate the typically larger forces that result from the shorter lattice spacing [22]. The anisotropy in step size requires a small amount of manual fine-tuning, but should be similar to the anisotropy in the lattice spacings.

Our base integration scheme in this work is due to Omelyan [34,35]; we use the combined update operator

$$\mathcal{U}^1(\delta\tau) = \mathcal{U}_p(\lambda\delta\tau)\mathcal{U}_q(\tfrac{1}{2}\delta\tau)\mathcal{U}_p(1 - 2\lambda\delta\tau)\mathcal{U}_q(\tfrac{1}{2}\delta\tau)$$
$$\times \mathcal{U}_p(\lambda\delta\tau), \qquad (15)$$

which results in a scheme that is clearly reversible and is accurate to $O(\delta\tau^3)$. The size of the leading error term can be further minimized by tuning the parameter λ. In our work we used the value of λ from Ref. [35] without any further tuning, which promises an efficiency increase of approximately 50% over the simple leapfrog algorithm.

In Refs. [32,36] it was shown that a reversible, multi-level integration scheme can be constructed which allows various pieces of the Hamiltonian to be integrated at different time scales. Let us consider a Hamiltonian of the form

$$H(\pi, U) = \tfrac{1}{2}\pi^\dagger_\mu(x)\pi_\mu(x) + S_1(U) + S_2(U), \qquad (16)$$

where $S_1(U)$ and $S_2(U)$ are pieces of the action with corresponding MD forces F_1 and F_2, respectively. One can then split the integration into two time scales. One can integrate with respect to action $S_1(U)$ using $\mathcal{U}^1(\delta\tau_1)$, where in the component $\mathcal{U}_p(\delta\tau_1)$ we use only the force F_1. The whole system can then be integrated with the update

$$\mathcal{U}^2(\delta\tau_2) = \mathcal{U}'_p(\lambda\delta\tau_2)\mathcal{U}^1(\tfrac{1}{2}\delta\tau_2)\mathcal{U}'_p(1 - 2\lambda\delta\tau_2)$$
$$\times \mathcal{U}^1(\tfrac{1}{2}\delta\tau_2)\mathcal{U}'_p(\lambda\delta\tau_2), \qquad (17)$$

where in $\mathcal{U}'_p$ we update the momenta using only F_2. Thus we end up with two characteristic integration time scales $\delta\tau_1$ and $\delta\tau_2$. The scheme generalizes recursively to a larger number of scales. A criterion for tuning the algorithm is to arrange for terms in the action to be mapped to different time scales so that on two time scales i and j we have $||F_i||\delta\tau_i \approx ||F_j||\delta\tau_j$, as suggested in Ref. [31]. We now proceed to outline how we split our action.

We can write our gauge action schematically as

$$S = S_s(U) + S_t(U), \qquad (18)$$

where the term S_s contains only loops with spatial gauge links, and the S_t term contains loops with spatial and temporal links. While the term S_s produces forces only in the spatial directions, the S_t term produces forces in both the spatial and the temporal directions. In particular, the spatial forces from S_t are larger in magnitude than the spatial forces from S_s by roughly the order of the anisotropy, and in turn, the temporal forces from S_t are larger than the spatial forces from S_t. Our anisotropic integration step size balances the spatial and temporal forces of the S_t term against each other. However, in order to balance the spatial forces from S_t and S_s against each other, we integrate them on separate time scales.

C. Mass preconditioning

Following the work of [31] our fermion determinant for the two-flavor simulation can be written as

$$\det(Q^\dagger Q) = \frac{\det(Q^\dagger Q)}{\det(Q_h^\dagger Q_h)}\det(Q_h^\dagger Q_h), \qquad (19)$$

where Q is the fermion matrix with our desired fermion mass m and Q_h is the fermion matrix for which we choose a heavier fermion mass m_h. After introducing pseudofermions the fermion action can be written as

$$S_f = S_f^1 + S_f^2, \qquad (20)$$

where

$$S_f^1 = \phi_1^\dagger Q_h(Q^\dagger Q)^{-1}Q_h^\dagger\phi_1, \qquad (21)$$

$$S_f^2 = \phi_2^\dagger(Q_h^\dagger Q_h)^{-1}\phi_2. \qquad (22)$$

This trick introduces two main advantages: first, because Q_h is heavier than Q, inversion in S_f^2 will take fewer iterations than solving with Q directly, and forces resulting from Q_h will likewise be smaller than those that would result from Q allowing slightly longer time steps; second, as long as m is not very different from m_h, we have that to first order $Q_h(Q^\dagger Q)^{-1}Q_h^\dagger \approx 1 + \Delta$ and that fluctuations with gauge fields will be to first order given by $\frac{\delta\Delta}{\delta U}$. It should be clear that as $m_h \to m$ we have $\Delta \to 0$, and that the resulting force $F \to 0$, in other words, that the magnitude of the force from S_f^1 can be made small in a controlled manner. The result is that while the inversions in S_f^1 are performed with Q and can be quite costly, by choosing m_h appropriately the force from S_f^1 can be reduced so that S_f^1 can be put on a long time scale and evaluated relatively infrequently during an MD trajectory. Some amount of effort is required to tune m_h so that the number of force evaluations from S_f^1 can be suitably reduced, while at the same time keeping m_h heavy enough, so that the force evaluations and inversions from S^2 do not become overly expensive.

D. Chronological inversion methods

In order to further reduce our inversion costs, we employ chronological guesses in our MD. Before every new solve we produce a chronological guess by employing the minimal residual extrapolation (MRE) method of [33]. This method works by using the last n solution vectors, which are orthonormalized with respect to each other to create an n dimensional basis. Let us denote these basis vectors v_i. The new initial guess v_g is then constructed as

$$v_g = \sum_i a_i v_i \qquad i = 1\cdots n, \qquad (23)$$

where a_i are coefficients to be determined given the constraint that the resulting v_g minimize the functional minimized by the conjugate gradients process in the subspace spanned by v_i:

$$\Psi[v_g] = v_g^\dagger Q^\dagger Q v_g - \chi^\dagger v_g - v_g^\dagger \chi, \qquad (24)$$

where χ is the right-hand side of the linear system for which the initial guess is being generated. Minimizing the functional Ψ with respect to a_i leads to the following set of linear equations for a_i:

$$\sum_{i=1}^{N} (v_j^\dagger Q^\dagger Q v_i) a_i = v_j^\dagger \chi. \qquad (25)$$

We emphasize that the use of chronological solution methods introduces reversibility violations into the MD evolution, and so the equations must be solved essentially exactly to avoid the reversibility violations from becoming large, and affecting the detailed balance condition and thereby biasing the Monte Carlo Markov process. To this end in our simulations we required a relative stopping residuum of

$$r_{MD} = \frac{\|\chi - (Q^\dagger Q)\phi\|}{\|\chi\|} < 10^{-8}. \qquad (26)$$

E. Summary

In summary, our HMC algorithm uses a Hamiltonian composed of the kinetic piece, the two gauge action pieces S_s and S_t, and the two fermion action pieces S_f^1 and S_f^2. Our molecular dynamics evolution uses a 2nd order Omelyan integrator split over three time scales:

(i) Time scale 1 is the slowest, with time step $\delta\tau_1$, and is used to evolve the Hasenbusch ratio term with action S_f^1;

(ii) time scale 2 is faster, with time step $\delta\tau_2$, and it is used to evolve the mass preconditioned fermion term with action S_f^2 and the spatial gauge term with action S_s;

(iii) time scale 3 is the fastest, with time step $\delta\tau_3$, and it is used to evolve the temporal gauge term with action S_t.

Our overall MD trajectory length is set to be $\tau = 1.0$. In addition at all levels of the integrator, the spatial time step on that level is a factor of $\xi_{MD} = 2.4$ larger than the temporal step. Both fermionic terms use the MRE chronological guess technique with up to $n = 8$ previous solutions. These preconditioning masses m_h and the concrete step sizes are summarized in Table I.

The acceptance rates were typically between 60% and 70%. The simulations at mass $m = -0.4125$ made use of the QCDOC supercomputer [14], as well as the BlueGene Teragrid Resource at San Diego Supercomputer Center, while the entire $m = -0.4086$ data set was generated on

TABLE I. The preconditioning masses m_h and the time steps used in the Omelyan integration scheme in our simulations, for each target sea quark mass m_0. Except for time scale 1, the time step for each time scale is given relative to the previous one. Trajectories are of length $\tau = 1$, with a step size anisotropy of $\xi_{MD} = 2.4$. The target solver residuum was $r = 10^{-8}$ for both MD and energy calculations and each fermionic term employed the MRE chronological guess method with up to the last eight previous vectors.

β	m_0	m_h	$\delta\tau_1$	$\frac{\delta\tau_2}{\delta\tau_1}$	$\frac{\delta\tau_3}{\delta\tau_2}$
5.5	−0.4086	−0.3700	$\frac{1}{4}$	$\frac{1}{2}$	$\frac{1}{3}$
5.5	−0.4125	−0.3740	$\frac{1}{4}$	$\frac{1}{4}$	$\frac{1}{3}$

Jaguar, a Cray XT3 resource at the National Center for Computational Science at Oak Ridge National Laboratory through the INCITE'07 program. The HMC algorithm with the various improvements discussed in this section is implemented and is freely available as part of the CHROMA software system [23].

TABLE II. Meson interpolating operators. The indicated charge-conjugation (C) quantum numbers apply only to particles with zero net flavor.

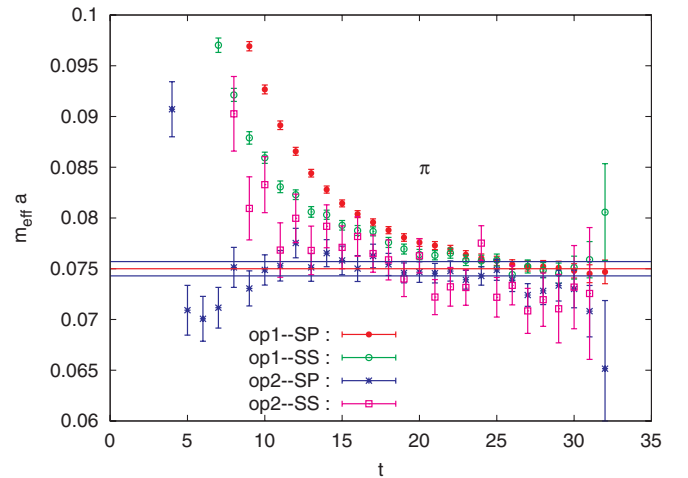| J^{PC}	Γ	$I = 1$
0^{-+}	γ_5	π
1^{--}	γ_μ	ρ
0^{++}	1	a_0
1^{++}	$\gamma_\mu \gamma_5$	a_1
1^{+-}	$\gamma_\mu \gamma_\nu$	b_1

FIG. 1 (color online). Pion effective mass results for different smearings (S denotes smeared, P denotes point) and operators (op1 denotes operators of Table II and op2 denotes operators including an extra factor of γ^4). Results are based on 862 gauge configurations, quark mass parameter $m_0 = -0.4125$, and a $24^3 \times 64$ lattice.

TABLE III.   Meson masses (in temporal lattice units) for $N_f =$ 2 with light quark mass $m_0 a_t = -0.4125$ based on 862 configurations. Columns 1 and 2 label the sources and sinks as smeared (S) or point (P) and the correlation functions based on the operators of Table II (S_1 or P_1), or based on including an extra factor γ^4 in the operators of Table II (S_2 or P_2). Simultaneous fits are performed for two types of operators in the results of rows 5 and 6. Fits are performed in time windows of $t = 26$ to $t = 32$ with $\chi^2/\mathrm{DOF} = 0.45(15)$ for the π meson.

Source	Sink	m_π	m_ρ
S	P_1	0.0754(5)	
S	S_1	0.0748(5)	0.1430(7)
S	P_2	0.0747(7)	0.1438(10)
S	S_2	0.0747(5)	0.1427(8)
S	$P_1\&P_2$	0.0753(5)	0.1431(7)
S	$S_1\&S_2$	0.0747(5)	0.1427(8)
Results		0.0750(7)	0.1431(8)

TABLE IV.   Meson masses (in temporal lattice units) for $N_f =$ 2 with quark mass $m_0 a_t = -0.4086$ based on 363 configurations. Notation is the same as in Table III. Fits are performed in time windows of $t = 26$ to $t = 32$ with $\chi^2/\mathrm{DOF} = 0.45(15)$ for the π meson.

Source	Sink	m_π	m_ρ
S	P_1	0.1088(7)	0.1668(12)
S	S_1		0.1652(13)
S	P_2	0.1088(12)	0.1680(13)
S	$P_1\&S_1$		0.1670(11)
S	$P_1\&P_2$	0.1088(7)	
Results		0.1088(8)	0.1668(16)

IV. CONVENTIONAL SPECTROSCOPY

A. Meson spectrum

We use meson interpolating fields of the form $\bar{\psi}\Gamma\psi$ and $\bar{\psi}\Gamma\gamma^4\psi$ that overlap with the physical states listed in Table II. Correlation functions are calculated and we fit them with the analytical function,

$$C(t) = A(e^{-mt} + e^{-m(T-t)}), \qquad (27)$$

where m is the mass parameter and T is the time extent of the lattice. Results for the mass parameters obtained from the fits of the correlations functions are summarized in Tables III and IV. Comparisons of the fits for the π meson with the effective mass are shown in Fig. 1 for the case of quark mass parameter $m_0 a_t = -0.4125$. Horizontal lines show the corresponding pion-mass parameter of the fits and the error band.

The fermion anisotropy ξ_f is determined through the conventional relativistic meson dispersion relation:

$$E^2(\mathbf{p}) = m^2 + \frac{\mathbf{p}^2}{\xi_f^2}, \qquad (28)$$

where the energy $E(\mathbf{p})$ and the mass m are in units of a_t, and $\mathbf{p} = \frac{2\pi\mathbf{n}}{L_s}$ where L_s is the spatial lattice size in units of a_s. From the two-point correlation functions we calculate the energy E at the spatial momenta $\mathbf{p} = \frac{2\pi\mathbf{n}}{L_s}$ for $\mathbf{n} = (0, 0, 0)$, $(1, 0, 0)$, $(1, 1, 0)$, and $(2, 0, 0)$ (averaged). The fitted jackknife energies are used in a linear fit of $E^2(\mathbf{p})$ as a function of $\mathbf{p}^2$ as in Eq. (28) in order to extract ξ_f. Figure 2 shows the dispersion relations for π and ρ mesons. The fitted values of ξ_f are 2.979(28) (with first three momenta fit) for the π meson and 3.045(35) (with first four momenta fit) for the rho meson. The central line shows the fit and the bands show the errors. The desired fermion anisotropy matches the gauge anisotropy, ξ_g, which is 3 in our case.
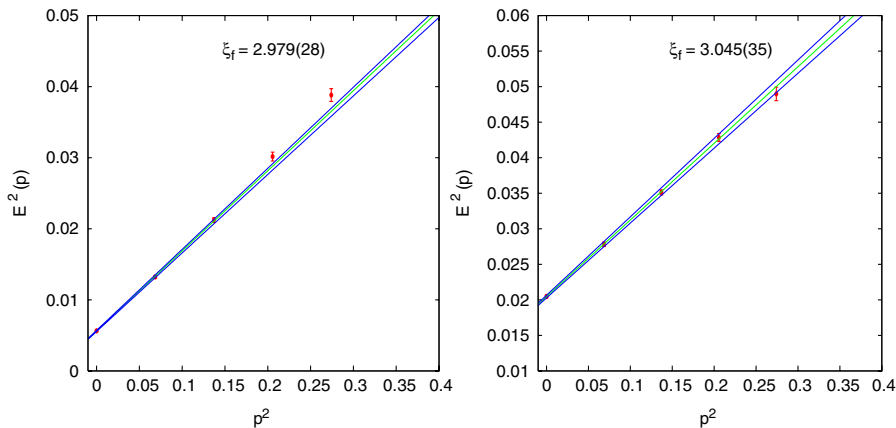

FIG. 2 (color online).   Dispersion relation for π (left panel) and ρ (right panel) mesons for quark mass parameter $m_0 = -0.4125$ and $24^3 \times 64$ lattice.

V. SCALE SETTING

In order to set the scale, the heavy-quark (static) potential $V(r)$ is calculated on a $16^3 \times 64$ lattice. This is expected to have the form

$$V(r) = C + \frac{\alpha}{r} + \sigma r, \qquad (29)$$

where r is the separation between the static quarks. The scale implied by the heavy-quark potential is often specified using the Sommer parameter r_0 which is defined by the condition

$$-r^2 \frac{\partial V(r)}{\partial r} \bigg|_{r=r_0} = 1.65. \qquad (30)$$

On the lattice, we calculate Wilson loops which determine the static-quark potential via

$$W(r, t) = Ae^{-V(r)t}. \qquad (31)$$

In order to improve the signal and to extract the potential $V(r)$ from smaller time separations, we smear the gauge links in the spatial directions using stout smearing with parameters $n_\rho = 16$, $n_\rho \rho = 2.5$. We fit the Wilson loops as a function of t at each available r to determine $V(r)$. We further fit $V(r)$ to determine C, α and σ according to Eq. (29) using a standard jackknife procedure. Putting these parameters back into Eq. (30), we solve for r_0/a_s.

Finally, we relate this to the physical scale by using the value $r_0 = 0.462(11)(4)$ fm from Refs. [37,38] and set the scale a_s. The results are summarized in Table V.

VI. BARYON OPERATORS

The use of operators whose temporal correlation functions attain their asymptotic form as quickly as possible is crucial for reliably extracting excited hadron masses. An important ingredient in constructing such hadron operators is the use of smeared fields. Operators constructed from smeared fields have dramatically reduced mixings with the high frequency modes of the theory. Both link smearing and quark-field smearing are necessary. Since excited hadrons are expected to be large objects, the use of spatially extended operators is another key ingredient in the operator design and implementation.

A. Smearing

Spatial links can be smeared using the stout-link procedure described in Ref. [39]. The stout-link smearing scheme is analytic, efficient, and produces smeared links that automatically are elements of $SU(3)$ without the need for a projection back into $SU(3)$. Note that only spatial staples are used in the link smoothing; no temporal staples are used, and the temporal link variables are not smeared. The smeared quark fields can be defined by

$$\tilde{\psi}(x) = \left(1 + \frac{\sigma_s^2}{4n_\sigma} \tilde{\Delta}\right)^{n_\sigma} \psi(x), \qquad (32)$$

where σ_s and n_σ are tunable parameters (n_σ is a positive integer) and the three-dimensional covariant Laplacian operators are defined in terms of the smeared link variables $\tilde{U}_j(x)$ as follows:

$$\tilde{\Delta} O(x) = \sum_{k=\pm 1, \pm 2, \pm 3} (\tilde{U}_k(x)O(x + \hat{k}) - O(x)), \qquad (33)$$

where $O(x)$ is an operator defined at lattice site x with appropriate color structure, and noting that $\tilde{U}_{-k}(x) = \tilde{U}_k^\dagger(x - \hat{k})$. The smeared fields $\tilde{\psi}$ and $\tilde{\bar{\psi}}$ are Grassmann valued; in particular, these fields anticommute in the same way that the original fields do, and the square of each smeared field vanishes.

B. Group theory

Hadron states are identified by their momentum $\boldsymbol{p}$, intrinsic spin J, projection λ of this spin onto some axis, parity $P = \pm 1$, and quark flavor content (isospin, strangeness, etc.). Some mesons also include G-parity as an identifying quantum number. If one is interested only in the masses of these states, one can restrict attention to the $\boldsymbol{p} = \boldsymbol{0}$ sector, so operators must be invariant under all spatial translations allowed on a cubic lattice. The little group of all symmetry transformations on a cubic lattice which leave $\boldsymbol{p} = \boldsymbol{0}$ invariant is the octahedral point group O_h, so operators may be classified using the irreducible representations (irreps) of O_h. For mesons, there are ten irreducible representations $A_{1g}, A_{2g}, E_g, T_{1g}, T_{2g}, A_{1u}, A_{2u}, E_u, T_{1u}$, and T_{2u}. The representations with a subscript $g(u)$ are even (odd) under parity. The A irreps are one dimensional, the E irreps are two dimensional, and the T irreps are three dimensional. The A_1 irreps contain the $J =$

TABLE V. The value of the Sommer parameter, r_0, is listed in column 1 and the ratio r_0/a_s for each quark mass on our $16^3 \times 64$ lattices is listed in column 3. The scale obtained from $r_0/(r_0/a_s)$ is listed in column 4. Using the renormalized anisotropy $\xi = 3$, we find the temporal spacing a_t^{-1} as given in column 5. The pion mass in lattice units is given in column 6 and in MeV units in column 7, while the bare anisotropy ξ_0 is given in column 8.

r_0 (fm)	$m_l a_t$	r_0/a_s	a_s (fm)	a_t^{-1} (MeV)	$m_\pi a_t$	m_π (MeV)	ξ_0
0.462(11)(4)	-0.4086	4.10(8)	0.113(7)	5310(265)	0.1088(37)	578(29)	2.38
0.462(11)(4)	-0.4125	4.26(12)	0.108(7)	5556(333)	0.0750(24)	416(36)	2.38

$0, 4, 6, 8, \ldots$ states, the A_2 irreps contain the $J = 3, 6, 7, 9, \ldots$ states, the E irreps contain the $J = 2, 4, 5, 6, 7, \ldots$ states, the T_1 irreps contain the spin $J = 1, 3, 4, 5, \ldots$ mesons, and the T_2 irreps contain the spin $J = 2, 3, 4, 5, \ldots$ states. For baryons, there are four two-dimensional irreps G_{1g}, G_{1u}, G_{2g}, and G_{2u} and two four-dimensional representations H_g and H_u. The G_1 irrep contains the $J = \frac{1}{2}, \frac{7}{2}, \frac{9}{2}, \frac{11}{2}, \ldots$ states, the H irrep contains the $J = \frac{3}{2}, \frac{5}{2}, \frac{7}{2}, \frac{9}{2}, \ldots$ states, and the G_2 irrep contains the $J = \frac{5}{2}, \frac{7}{2}, \frac{11}{2}, \ldots$ states. The continuum-limit spins J of our states must be deduced by examining degeneracy patterns across the different O_h irreps.

C. Operator construction and pruning

Our operators are constructed in a three-stage approach [3]. First, basic building blocks are chosen. These are taken to be smeared covariantly displaced quark fields

$$(\tilde{D}_j^{(p)} \tilde{\psi})_{a\alpha}^A, \qquad (\tilde{\bar{\psi}} \tilde{D}_j^{(p)\dagger})_{a\alpha}^A, \qquad -3 \le j \le 3, \quad (34)$$

where A is a flavor index, a is a color index, α is a Dirac spin index, and the p-link gauge-covariant displacement operator in the jth direction is defined by

$$\tilde{D}_j^{(p)}(x, x') = \tilde{U}_j(x)\tilde{U}_j(x + \hat{j}) \cdots \tilde{U}_j(x + (p-1)\hat{j})\delta_{x', x+p\hat{j}},$$

$$\tilde{D}_0^{(p)}(x, x') = \delta_{xx'}, \qquad (35)$$

for $j = \pm 1, \pm 2, \pm 3$, and $p \ge 1$, and where $j = 0$ defines a zero-displacement operator to indicate no displacement. Next, *elemental* operators $B_i^F(t, \boldsymbol{x})$ are devised having the appropriate flavor structure characterized by isospin, strangeness, etc., and color structure constrained by gauge invariance. For zero momentum states, translational invariance is imposed: $B_i^F(t) = \sum_{\boldsymbol{x}} B_i^F(t, \boldsymbol{x})$. Finally, group-theoretical projections are applied to obtain operators which transform irreducibly under all lattice rotation and reflection symmetries:

$$\mathcal{B}_i^{\Lambda\lambda F}(t) = \frac{d_\Lambda}{g_{O_h^D}} \sum_{R \in O_h^D} \Gamma_{\lambda\lambda}^{(\Lambda)}(R) U_R B_i^F(t) U_R^\dagger, \quad (36)$$

where O_h^D is the double group of O_h, R denotes an element of O_h^D, $g_{O_h^D}$ is the number of elements in O_h^D, and d_Λ is the

single　singly　doubly　doubly　triply　triply
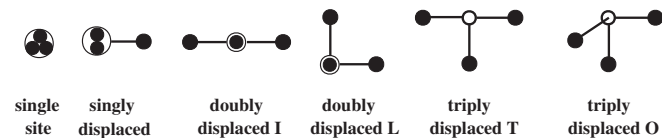site　displaced　displaced I　displaced L　displaced T　displaced O

FIG. 3.　The spatial arrangements of the extended three-quark baryon operators. Smeared quark fields are shown by solid circles, line segments indicate gauge-covariant displacements, and each hollow circle indicates the location of a Levi-Cività color coupling. For simplicity, all displacements have the same length in an operator. Results presented here used displacement lengths of $3a_s$ (~ 0.3 fm).

single　singly　doubly　triply　triply
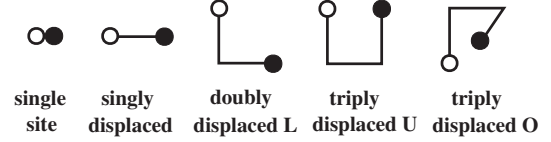site　displaced　displaced L　displaced U　displaced O

FIG. 4.　The spatial arrangements of the quark-antiquark meson operators. In the illustrations, the smeared quarks fields are depicted by solid circles, each hollow circle indicates a smeared "barred" antiquark field, and the solid line segments indicate covariant displacements.

dimension of the Λ irreducible representation. Projections onto both the single-valued and double-valued irreps of O_h require using the double group O_h^D in Eq. (36). Given M_B elemental B_i^F operators, many of the projections in Eq. (36) vanish or lead to linearly dependent operators, so one must then choose suitable linear combinations of the projected operators to obtain a final set of independent baryon operators. Thus, in each symmetry channel, one ends up with a set of r operators given in terms of a linear superposition of the M_B elemental operators. The different spatial configurations (see Fig. 3 for the baryon configurations and Fig. 4 for the meson configurations) yield operators which
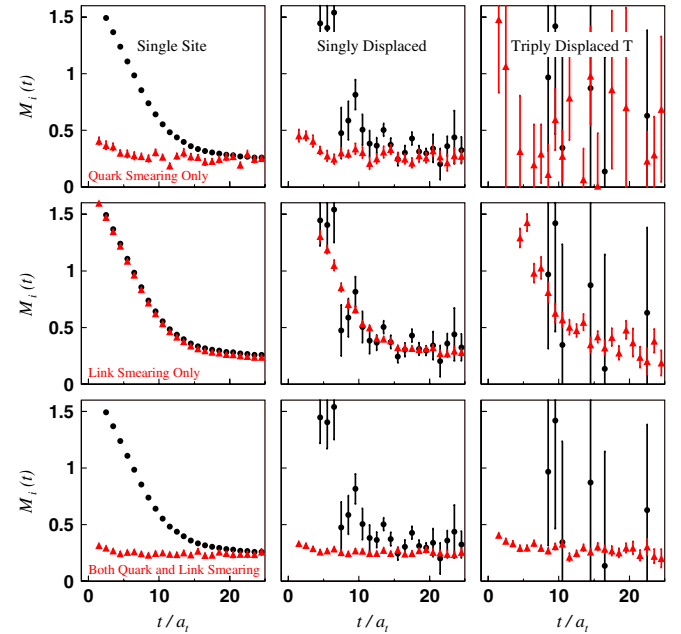

FIG. 5 (color online).　Effective masses $M(t)$ for unsmeared (black circles) and smeared (red triangles) operators O_{SS}, O_{SD}, and O_{TDT}, which are representative single-site, singly displaced, and triply displaced-T nucleon operators, respectively. Top row: only quark-field smearing $n_\sigma = 32$, $\sigma_s = 4.0$ is used. Middle row: only link-variable smearing $n_\rho = 16$, $n_\rho\rho = 2.5$ is applied. Bottom row: both quark and link smearing $n_\sigma = 32$, $\sigma_s = 4.0$, $n_\rho = 16$, $n_\rho\rho = 2.5$ are used, dramatically improving the signal for all three operators. Results are based on 50 quenched configurations on a $12^3 \times 48$ anisotropic lattice using the Wilson action with $a_s \sim 0.1$ fm, $a_s/a_t \sim 3.0$.

effectively build up the necessary orbital and radial structures of the hadron excitations. The design of these operators is such that a large number of them can be evaluated very efficiently, and components in their construction can be used for both meson, baryon, and multihadron computations.

Finding appropriate smearing parameters is a crucial initial part of any hadron spectrum calculation. Figure 5 demonstrates that *both* quark-field and link-field smearing are needed in order for spatially extended baryon operators to be useful [5]. It is important to use the smeared links when smearing the quark field. Link smearing dramatically reduces the statistical errors in the correlators of the displaced operators, while quark-field smearing dramatically reduces the excited-state contamination. In this study, the quark field is Gaussian smeared with $\sigma = 3.0$ using 32 iterations, and the link field is stout smeared with $n_\rho = 16$, $n_\rho \rho = 2.5$.

Our approach to designing hadron and multihadron interpolating fields leads to a very large number of operators. It is not feasible to do spectrum computations using all of the operators so designed; for example, in the G_{1g} symmetry channel for nucleons, the above procedure leads to 179 operators. It is necessary to *prune* down the number of operators. After much exploratory testing and trials, we found that a procedure that keeps a variety of operators while minimizing the effects of noise works best for facilitating the extraction of several excited states. Some operators are intrinsically noisy and must be removed. In addition, a set of operators, each with little intrinsic noise, can allow noise to creep in if they are not sufficiently independent of one another.

The following procedure was used. (1) First, operators with excessive intrinsic noise were removed. This was done by examining the diagonal elements of the correlation matrix and discarding those operators whose self-correlators had relative errors above some threshold for a range of temporal separations. A low-statistics Monte Carlo computation on a reasonably small lattice was used to accomplish this. (2) Second, pruning within operator types (single site, singly displaced, etc.) was done based on the condition number of the submatrices

$$\hat{C}_{ij}(t) = \frac{C_{ij}(t)}{\sqrt{C_{ii}(t)C_{jj}(t)}}, \qquad t = a_t.$$

The condition number was taken to be the ratio of the largest eigenvalue over the smallest eigenvalue. A value near unity is ideal. For each operator type, the set of about six operators which yielded the lowest condition number of the above submatrix was retained. (3) Lastly, pruning across all operator types was done based again on the condition number of the remaining submatrix as defined above. In this last step, the goal was to choose about 16 operators, keeping two or three of each type, such that a

condition number reasonably close to unity was obtained. As long as a good variety of operators was retained, the resulting spectrum seemed to be fairly independent of the exact choice of operators at this stage. Eigenvectors from a variational study of the operators could also be used to fine-tune the choice of operators.

VII. $I = \frac{1}{2}$ BARYON SPECTRA

Each of our unbarred (barred) baryon operators annihilates (creates) a baryon and creates (annihilates) an antibaryon. This causes correlation functions to have a baryon state propagating forward in time and an antibaryon state propagating backward in time. Because fermions and antifermions have opposite intrinsic parities, the backward-in-time signal corresponds to states with parity opposite to that of the states propagating forward in time. Because of PCT symmetry coupled with the use of antiperiodic boundary conditions, correlation functions obey the rule

$$C_{kk'}^{(\Lambda)}(t) = C_{kk'}^{(\Lambda_c)}(T - t)^*, \tag{37}$$

where Λ_c is the opposite-parity partner of irrep Λ. This allows us to increase our statistics by "folding" the correlation functions:

$$C_{kk'}^{(\Lambda)}(t) \rightarrow \tfrac{1}{2}(C_{kk'}^{(\Lambda)}(t) + C_{kk'}^{(\Lambda_c)}(T - t)^*). \tag{38}$$

Generally the separation of the two time slices involved is sufficient to provide independent samples of the gauge configurations.

We choose phases of our baryon operators such that the matrices of correlation functions are real. We also average the matrix with its transpose in order to guarantee that the matrices are symmetric. This helps to clean up the signals by reducing the errors.

A. The variational method

We calculated 16×16 matrices of correlation functions in each irrep of the octahedral group: $\Lambda = \{G_{1g}, G_{2g}, H_g, G_{1u}, G_{2u}, H_u\}$. The variational method was used to help extract the excited spectrum from the matrices of correlation functions, which involved numerically solving the generalized eigenvalue problem

$$C_{kk'}^{(\Lambda)}(t)v_{k'}^{(n)}(t, t_0) = \lambda_n^{(\Lambda)}(t, t_0)C_{kk'}^{(\Lambda)}(t_0)v_{k'}^{(n)}(t, t_0), \tag{39}$$

where n labels the eigenstates. Degeneracies and numerical uncertainties can cause variances of the eigenvectors at different times. We studied two methods for extracting the spectrum: (1) a fixed-eigenvector method and (2) a principal-correlator method where the diagonalizations were performed on each time step.

The fixed-eigenvector method involved solving the eigenvalue problem on a single time slice $t = t^*$ using a fixed value of t_0. These eigenvectors are normalized with respect to $C_{kk'}^{(\Lambda)}(t_0)$ such that

$$v_k^{(n)\dagger}(t^*, t_0) C_{kk'}^{(\Lambda)}(t_0) v_{k'}^{(n)}(t^*, t_0) = \delta_{kk'}. \qquad (40)$$

For each time slice and each configuration, the matrix of correlation functions was rotated to this basis of vectors using

$$\tilde{C}_{kk'}^{(\Lambda)}(t) = V_{kn}^\dagger(t^*, t_0) C_{nn'}^{(\Lambda)}(t) V_{n'k'}(t^*, t_0), \qquad (41)$$

where $V_{n'k'}(t^*, t_0)$ is the matrix whose columns are the eigenvectors at time t^*. Because of Eq. (40), the rotated matrices of correlation functions are equal to the identity matrix at time t_0.

The diagonal elements of the rotated correlation matrix are related to the energies by

$$\tilde{C}_{kk}^{(\Lambda)}(t) \simeq e^{-E_k(t-t_0)} + \sum_{n \neq k} \alpha_n e^{-E_n(t-t_0)} + \mathcal{O}(e^{-(E_{N+1}-E_k)t}), \qquad (42)$$

where the sum over terms involving α_n vanishes at time t^*, but can contribute away from t^*. The term involving the first omitted energy, E_{N+1}, has been derived by Blossier *et al.* [40]. We extract the low lying energies by performing fully correlated χ^2-minimization fits, modeling the kth diagonal element of the rotated correlator matrix as

$$\tilde{C}_{kk}^{\text{fit}}(t) = (1 - A)e^{-E_k(t-t_0)} + Ae^{-E'(t-t_0)}, \qquad (43)$$

where E_k is the energy of the kth state. The second exponential captures the contribution of the higher energy states and allows us to fit the correlators to early time slices. The choice of coefficients in front of each exponential enforces $\tilde{C}_{kk}^{\text{fit}}(t_0) = 1$, as guaranteed by Eq. (40). We assume that the α_n in Eq. (42) are negligible in the time range over which we perform the fit.

We optimized our choice of t_0 and t^* using a method adapted from that in Ref. [20]. In that work, the optimal choice of t_0 was determined for the extraction of the charmonium spectrum using a principal-correlator analysis. This optimal choice balanced the need for the contributions of higher energy states to have decayed away (suggesting larger values for t_0) and for the correlator to have a low level of noise (suggesting smaller values for t_0). The energies in the low lying spectrum were extracted by fitting the principal correlators for various values of t_0. For each value of t_0, the correlator was reconstructed from these fit energies and the eigenvectors using the spectral decomposition of the correlator matrix

$$C_{ij}(t) = \langle \mathcal{O}_i(t) \mathcal{O}_j(0) \rangle = \sum_\alpha \frac{Z_i^{\alpha*} Z_j^\alpha}{2m_\alpha} e^{-m_\alpha t}. \qquad (44)$$

The overlap factors $Z_i^\alpha = \langle 0 | \mathcal{O}_i | \alpha \rangle$ are related to the eigenvectors of the correlator by

$$Z_i^\alpha = (V^{-1})_i^\alpha \sqrt{2m_\alpha} e^{m_\alpha t_0/2}. \qquad (45)$$

A χ^2-like quantity was defined to measure how well the reconstructed correlator described the original correlator matrix:

$$\chi^2 = \frac{1}{\frac{1}{2}N(N+1)(t_{\max} - t_0) - \frac{1}{2}N(N+3)} \sum_{i,j \geq i} \sum_{t,t'=t_0+1}^{t_{\max}} (C_{ij}(t)$$
$$- C_{ij}^{\text{rec.}}(t)) \mathbb{C}_{ij}^{-1}(t, t')(C_{ij}(t') - C_{ij}^{\text{rec.}}(t')), \qquad (46)$$

where $\mathbb{C}_{ij}^{-1}(t, t')$ is the correlation matrix for the correlator C_{ij}. Although the principal-correlator method actually yields time dependent overlap factors $Z(t)$ (because the correlator matrix is diagonalized on all time slices), it was observed that the $Z(t)$ were reasonably constant and the reconstruction was done using a single $Z(t_Z)$ chosen at a time such that χ^2 was minimized. For $t_Z > t_0$, the variation in χ^2 as a function of t_Z was minimal.

In this work, we adapt this technique for the fixed-eigenvector method, finding optimal values for t_0 and t^*. We extract the 16 lowest energies in the spectrum by fitting the diagonal elements of the rotated correlator matrix, Eq. (41), obtained using a range of values for t_0 and t^*. Reconstructing the correlator from these masses and the Z factors at t^*, we choose the t_0 and t^* which minimize the χ^2.

To correctly extract the energy spectrum, it is also crucial to select an appropriate range of time slices on which to fit the correlator. In particular, we would like to avoid time slices where the opposite-parity backward-propagating state contributes to the correlator. For mesons, where the forward- and backward-propagating states have the same parity, the variational method simultaneously diagonalizes the forward- and backward-propagating parts of a meson correlation function. This is not the case for baryons where the forward- and backward-propagating states have opposite parities and different energies. The forward-in-time signals dominate at small values of time but they decay exponentially and the backward-propagating signals can become significant after some threshold value of time. We were able to extract the energies of the states by fitting the diagonal correlation functions using Eq. (43) without significant interference from the backward-propagating signal for all channels except G_{1u} at $m_\pi = 416$ MeV. In this channel, the backward-propagating signal is dominated by the G_{1g} ground state, which is the lowest energy state in the spectrum. For our lattice at the lower pion mass, the backward-propagating G_{1g} signal decayed slowly enough and the temporal extent was small enough (due to the anisotropy) that the G_{1u} signals had significant backward contamination even at small time slices. To extract the G_{1u} energy levels using the fixed-eigenvector method, we include the backward-propagating state in the fit and constrain its energy by fitting simultaneously the G_{1g} ground state:

$$C_k^{\text{fit},G_{1u}} = (1 - A - B)e^{-E_k^{G_{1u}}(t-t_0)} + Ae^{-E'(t-t_0)}$$
$$+ Be^{E_0^{G_{1g}}(t-t_0)}, \qquad (47)$$

$$C_0^{\text{fit},G_{1g}} = (1-D)e^{-E_0^{G_{1g}}(t-t_0)} + De^{-E''(t-t_0)}. \qquad (48)$$

Because of the increased noise in the excited states, the minimizer was unable to find a minimum in the χ^2 for these simultaneous fits for $k \geq 2$. We were able to successfully fit these states by modeling the forward-propagating state as single exponential and fitting only on later time slices (where the higher energy states had completely decayed).

The fit ranges were optimized such that the χ^2 was minimized. To visually confirm the sensibility of the fit parameters, we look at plots of

$$\tilde{C}_{kk}^{\Lambda}e^{E_k(t-t_0)}, \qquad (49)$$

versus time. If Eq. (43) correctly models the correlator, then the plot should plateau to $(1-A)$ and we confirm that the plateau is consistent with the value of A determined from the fit. For the G_{1u} channel at $m_\pi = 416$ MeV, we first subtract off the backward exponential and compare the plateau with $(1-A-B)$ as in Eq. (47). Finally, we confirm that the fit parameters are stable under small variations in the fit range. We estimate the uncertainty in the fit energy through a jackknife analysis. We fit each member of a jackknife ensemble to obtain an ensemble of energies and report the average energy and the jackknife error.

The presence of the backward-propagating state in the G_{1u} channel caused numerical instabilities in the eigenvectors of the principal-correlator method. In order to remove the cause of the problem, we tested a method based on filtering out the backward signal prior to diagonalization. In a time interval where the backward signal is simply the ground state of the opposite-parity channel with energy $E_0^{\Lambda_c}$, the matrix of correlation functions can be modeled as a forward part plus the single backward state,

$$C_{kk'}^{(\Lambda)}(t) = \sum_n A_{kk'}^{(n)} e^{-E_n^\Lambda(t-t_0)} + B_{kk'} e^{-E_0^{\Lambda_c}(T-t_0)}. \qquad (50)$$

We define the filtered correlator as

$$C_{\text{filt},kk'}^{(\Lambda)} = C_{kk'}^{(\Lambda)}(t) - C_{kk'}^{(\Lambda)}(t_1) + (1 - e_0^{-E^{\Lambda_c}}) \sum_{j=t+1}^{t_1} C_{kk'}^{(\Lambda)}(j), \qquad (51)$$

and find that it can be modeled as

$$C_{\text{filt},kk'}^{(\Lambda)} = \sum_n \tilde{A}_{kk'}^{(n)}(e^{-E_n^\Lambda(t-t_0)} - e^{-E_n^\Lambda(t_1-t_0)}),$$

$$\tilde{A}_{kk'}^{(n)} = A_{kk'}^{(n)}\left[1 + \frac{1 - e^{-E_0^{\Lambda_c}}}{e^{E_n^\Lambda} - 1}\right], \qquad (52)$$

where t_1 is a time where the backward signal is, in fact, described by single exponential. The backward-in-time signal for energy $E_0^{\Lambda_c}$ is reduced to the level of errors and the filtered correlators consist of the renormalized forward signal minus a constant term. The diagonalization of the filtered correlators using the principal-correlator method produced stable eigenvectors and the energies of the states could be extracted by fitting the principal correlation functions to a single exponential decay with a constant term. However, this method did not produce any significant improvement over the results from the fixed-eigenvector method. We point out that the filtering is necessary in order to extract the G_{1u} excited spectrum from our lattices using the principal-correlator method.

TABLE VI. Isospin $\frac{1}{2}$ spectrum for $m_\pi = 416$ MeV. The energies in MeV units are based on the scale $a_t^{-1} = 5556$ MeV and do not include the error in the determination of the scale that acts as an overall multiplicative factor in the range 0.94–1.06.

Time	G_{1g}, $t_0 = 7$, $t^* = 10$ Ea_t	E (MeV)	Time	G_{1u}, $t_0 = 7$, $t^* = 9$ Ea_t	E (MeV)
3–21	0.2044(18)	1136(10)	3–14	0.3146(61)	1748(34)
2–14	0.3747(126)	2082(70)	2–14	0.3343(67)	1857(37)
2–12	0.4177(137)	2321(76)	7–14	0.5014(136)	2786(76)
2–12	0.4201(277)	2334(154)	7–13	0.5238(158)	2910(88)
	H_g, $t_0 = 8$, $t^* = 10$			H_u, $t_0 = 8$, $t^* = 9$	
Time	Ea_t	E (MeV)	Time	Ea_t	E (MeV)
3–16	0.4004(74)	2225(41)	3–23	0.3208(87)	1782(48)
3–17	0.4146(126)	2304(70)	3–21	0.3320(86)	1845(48)
3–18	0.4193(120)	2330(67)	3–19	0.3535(87)	1964(48)
3–16	0.4144(202)	2302(112)	2–11	0.5157(174)	2865(97)
	G_{2g}, $t_0 = 6$, $t^* = 8$			G_{2u}, $t_0 = 6$, $t^* = 9$	
Time	Ea_t	E (MeV)	Time	Ea_t	E (MeV)
2–12	0.4448(122)	2471(68)	2–17	0.3523(92)	1957(51)
2–12	0.4593(104)	2552(58)	2–12	0.5035(119)	2797(66)
2–11	0.4659(110)	2589(61)	2–12	0.5373(162)	2985(90)
2–14	0.4796(127)	2665(71)	2–10	0.5446(131)	3026(73)

TABLE VII.   Isospin $\frac{1}{2}$ spectrum for $m_\pi = 578$ MeV. The energies in MeV units are based on the scale $a_t^{-1} = 5310$ MeV, and do not include the error in the scale determination that acts as an overall multiplicative factor in the range 0.95–1.05.

| | G_{1g}, $t_0 = 6$, $t^* = 10$ | | | G_{1u}, $t_0 = 6$, $t^* = 9$ | |
Time	Ea_t	E (MeV)	Time	Ea_t	E (MeV)
2–27	0.2463(17)	1308(9)	2–11	0.3719(48)	1975(25)
2–15	0.4291(110)	2279(58)	2–11	0.3811(56)	2024(30)
2–15	0.4643(116)	2465(62)	2–11	0.5186(141)	2754(75)
2–11	0.4631(123)	2459(65)	2–11	0.5431(121)	2884(64)
	H_g, $t_0 = 6$, $t^* = 9$			H_u, $t_0 = 5$, $t^* = 7$	
Time	Ea_t	E (MeV)	Time	Ea_t	E (MeV)
2–14	0.4450(90)	2363(48)	2–11	0.3802(86)	2019(46)
2–11	0.4789(96)	2543(51)	2–11	0.3975(89)	2111(47)
2–11	0.4758(95)	2526(50)	2–11	0.4110(72)	2182(38)
2–11	0.4996(99)	2653(53)	2–11	0.5670(215)	3011(114)
	G_{2g}, $t_0 = 5$, $t^* = 9$			G_{2u}, $t_0 = 5$, $t^* = 9$	
Time	Ea_t	E (MeV)	Time	Ea_t	E (MeV)
2–15	0.4422(144)	2348(76)	2–11	0.4017(81)	2133(43)
2–15	0.4887(113)	2595(60)	2–11	0.5223(188)	2773(100)
2–12	0.5030(94)	2671(50)	2–11	0.5399(139)	2867(74)
2–14	0.5035(108)	2674(57)	2–11	0.5601(142)	2974(75)

B. Results

We extracted spectra using the fixed-eigenvector method from the $m_\pi = 416$ MeV lattice using 430 gauge configurations and from the $m_\pi = 578$ MeV lattice using 363 gauge configurations. Four states are reported for each channel for both pion masses. The results for $m_\pi = 416$ MeV are given in Table VI and the results for $m_\pi = 578$ MeV are given in Table VII. The results are based on 16×16 matrices of correlation functions using values of t_0, t^* and the fitting windows $t_i - t_f$ as shown in the tables.

Plots of the $N_f = 2$ spectrum for the two m_π values are shown in Fig. 6. The pion mass is shown by the dashed line and thresholds for multiparticle states (to be discussed further on) are shown by empty boxes. Plots of Eq. (49) versus time for each extracted state are shown in Figs. 7–12.

In the positive-parity channels, we identify the G_{1g} ground state as the nucleon. The spectrum for $m_\pi = 416$ MeV is shifted toward higher energy values for $m_\pi = 578$ MeV. The nucleon mass increases 172 MeV from
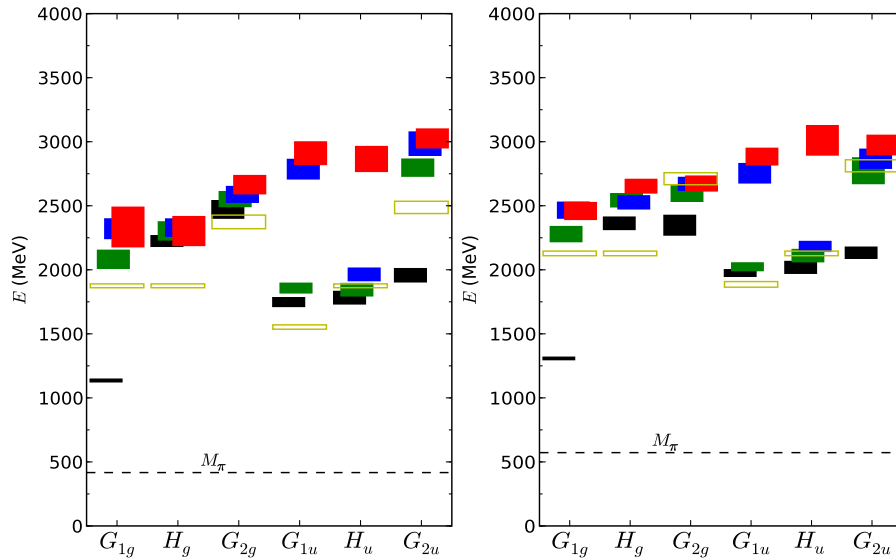

FIG. 6 (color online).   The energies obtained for each symmetry channel of isospin $\frac{1}{2}$ baryons are shown based on the $24^3 \times 64$ $N_f = 2$ lattice QCD data for $m_\pi = 416$ MeV (left panel) and $m_\pi = 578$ MeV (right panel). The scale shows energies in MeV and errors are indicated by the vertical size of the boxes. The overall error in the scale setting is not included. Empty boxes show thresholds for multihadron states.
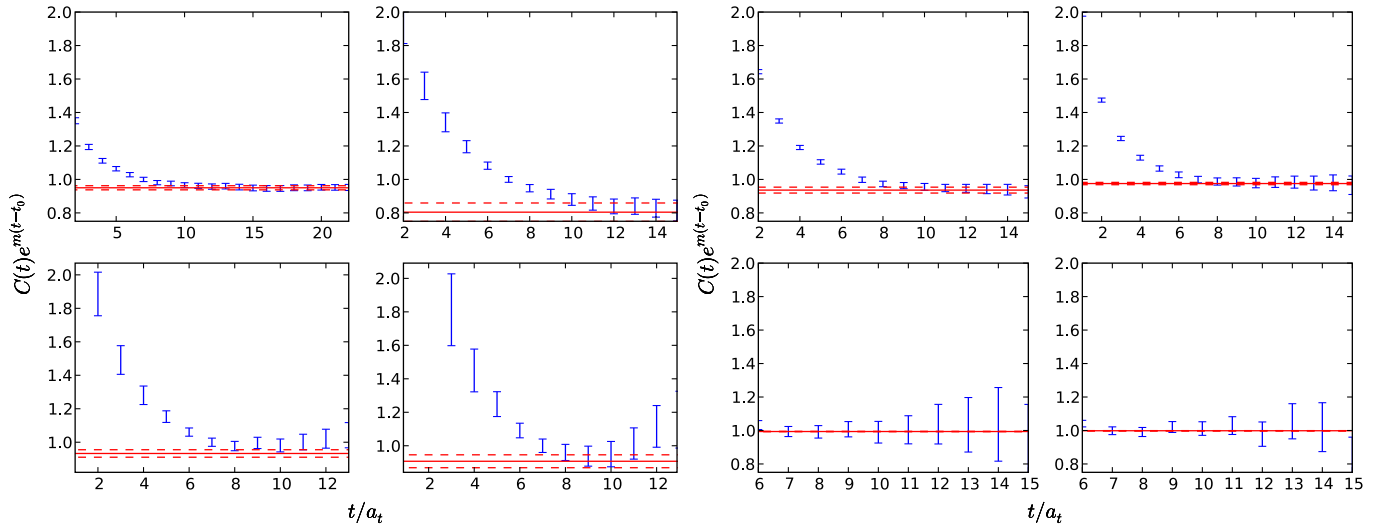
FIG. 7 (color online).   Plots of Eq. (49) versus time for G_{1g} states (left panels) and G_{1u} states (right panels) for $m_\pi = 416$ MeV. For the two lowest energy states in the G_{1u} channel we first subtract off the backward exponential.

1136 to 1308 MeV when m_π increases 162 MeV. If we extrapolate the nucleon to the physical pion mass using the formula $M = a + bm_\pi^2$, the result is 972(28) MeV.

Results for the negative-parity excited states exhibit some interesting features. The pattern of G_{1u} energies shows two states at approximately 1.5 and 1.6 times the nucleon mass with the next state much higher. This pattern is similar to the pattern of masses of the physical spectrum, which has $\frac{1}{2}^-$ resonances at 1535 and 1650 MeV with the third $\frac{1}{2}^-$ resonance well above them at 2090 MeV. Because our baryon operators do not contain multihadron operators, they are expected to couple more strongly to three-quark states, suggesting that the lowest G_{1u} state is more likely to be a N^* state. However, it is above the threshold for a πN scattering state so further analysis clearly is needed to confirm this assignment.

An isolated state in the H_u irrep corresponds to a spin $\frac{3}{2}^-$ state for which the lowest physical state is the $N(1520)$ resonance and the next to lowest is the $N(1700)$. In the H_u channel, the energies of the three lowest states are about 1.57, 1.62, and 1.73 times the nucleon mass at the lower pion mass. The physical states for spin $\frac{3}{2}^-$ are 1.62 and 1.81 times the physical nucleon mass. In the G_{2u} channel at $m_\pi = 416$ MeV, we see that the lowest energy state at 1957(51) MeV is degenerate (within errors) with the third H_u state at 1964(48) MeV with no state at the same energy in the G_{1u} channel. A similar pattern is seen for $m_\pi = 578$ MeV, except shifted upward by about 190 MeV. The lowest G_{2u} state at 2133(43) MeV is degenerate with the third H_u state at 2182(38) MeV. This pattern is the signature of a spin $\frac{3}{2}^-$ state and a nearby spin $\frac{5}{2}^-$ state. One H_u
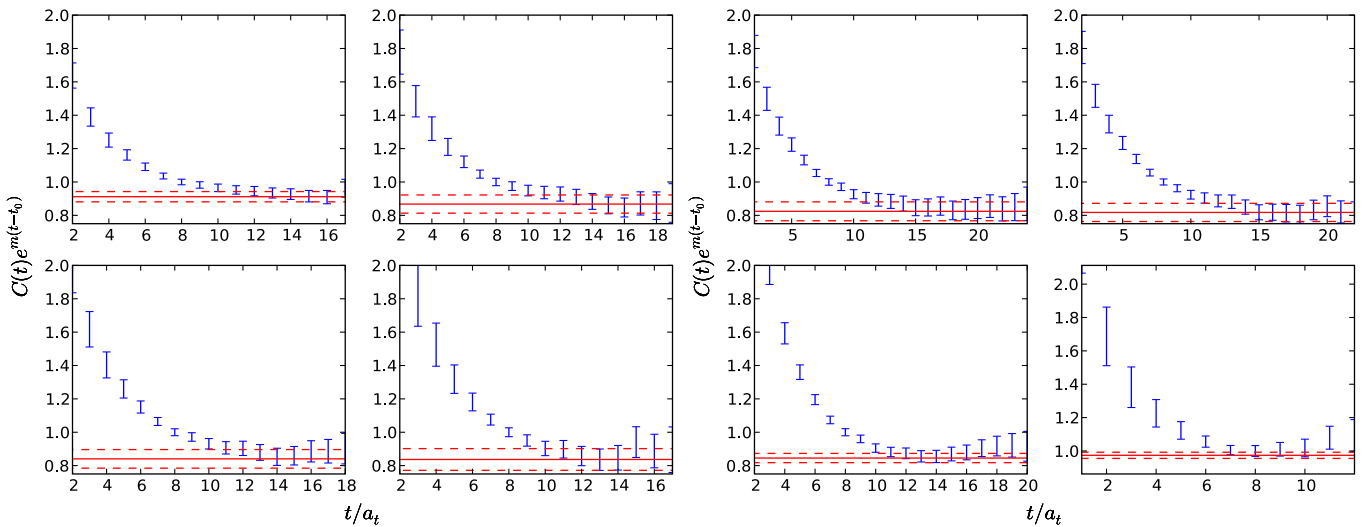

FIG. 8 (color online).   Plots of Eq. (49) versus time for H_g states (left panels) and H_u states (right panels) for $m_\pi = 416$ MeV.
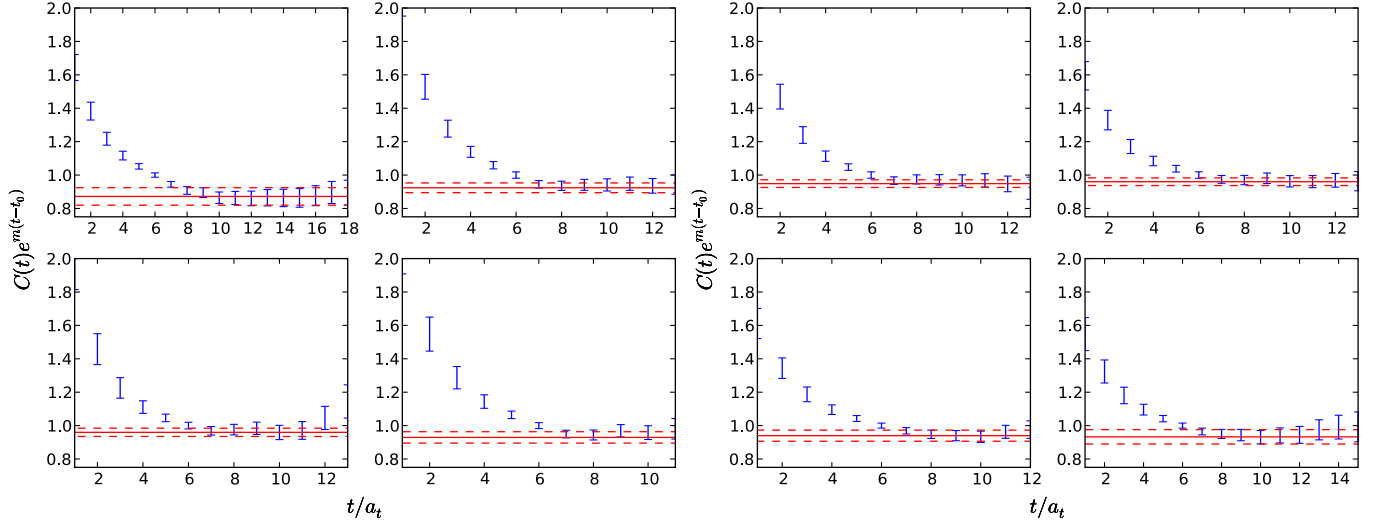
FIG. 9 (color online).   Plots of Eq. (49) versus time for G_{2g} states (left panels) and G_{2u} states (right panels) for $m_\pi = 416$ MeV.

state, most likely the second, is the spin $\frac{3}{2}^-$ state and the other H_u state is the partner state of the G_{2u} state required for a spin $\frac{5}{2}^-$ state. The lowest possible spin in G_{2u} is $\frac{5}{2}$ and because the G_{2u} irrep has only two of the $2J + 1 = 6$ components needed for spin $\frac{5}{2}$, the other four components necessarily are in a partner H_u state. For a spin $\frac{5}{2}$ state, the G_{2u} and H_u states must be degenerate in the continuum limit and for a clean interpretation there should not be a G_{1u} state that is degenerate with these two because that would be the signature of an isolated spin $\frac{7}{2}$ state or a possible accidental degeneracy of a spin $\frac{1}{2}$ and $\frac{5}{2}$ states. Our spectra show evidence for a spin $\frac{5}{2}$ state and a spin $\frac{3}{2}$ state close to the same energy. As the pion mass is reduced to 140 MeV and the lattice spacing is extrapolated to zero, the partner H_u and G_{2u} states in the lattice spectrum should approach the lowest $\frac{5}{2}^-$ state in the physical spectrum, i.e., $N(1675)$ with a half-width of 75 MeV. The first and second

H_u states should approach the 1520 and 1700 MeV spin $\frac{3}{2}^-$ states in the physical spectrum.

The first excited positive-parity state in G_{1g} is at 2082 (70) MeV for the lighter pion mass. That is 1.83 times the mass of the lowest G_{1g} state (nucleon) and about 334 MeV more massive than the lowest G_{1u} state. It also is well above the threshold energy for a p-wave $N\pi$ state (1785 MeV at the 416 MeV pion mass and this lattice length). In the physical spectrum the first excited, even-parity resonance is $N(1440)\frac{1}{2}^+$ with energy 1.53 times the nucleon mass and below that of the lowest odd-parity $N^*(1535)\frac{1}{2}^-$ state. Whether the energy of the first excited G_{1g} state will decrease toward the Roper state at lower values of the pion mass remains an open question.

A signal for a $\frac{5}{2}^-$ state could not be clearly identified in the quenched QCD analysis of Ref. [6] at 480 MeV pion mass. That spectrum had larger errors and showed three
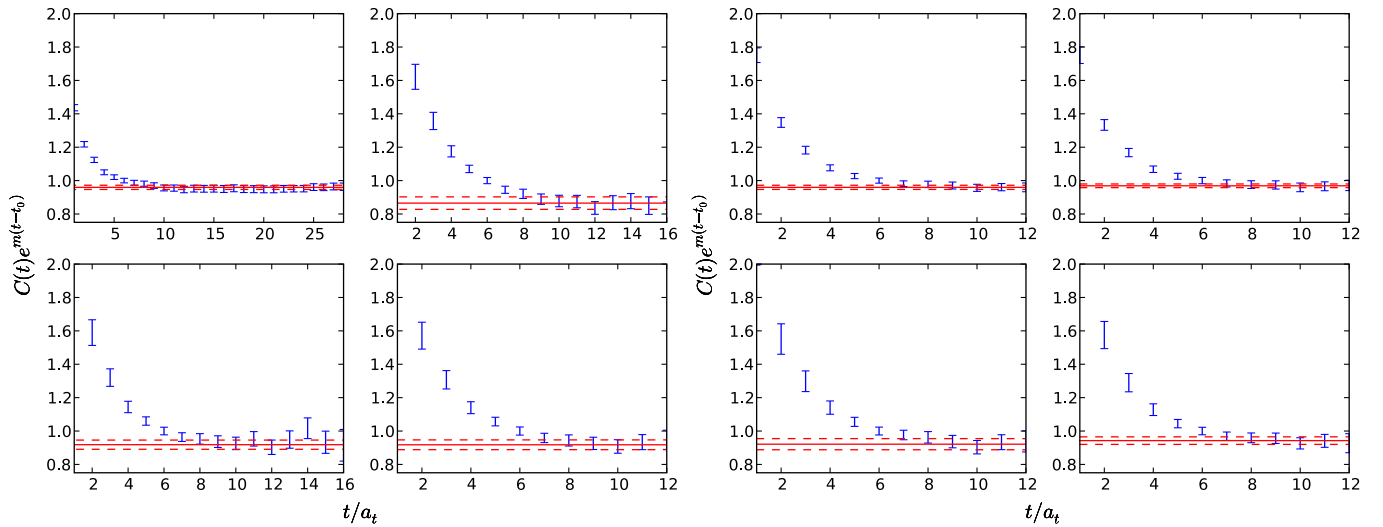

FIG. 10 (color online).   Plots of Eq. (49) versus time for G_{1g} states (left panels) and G_{1u} states (right panels) for $m_\pi = 578$ MeV.
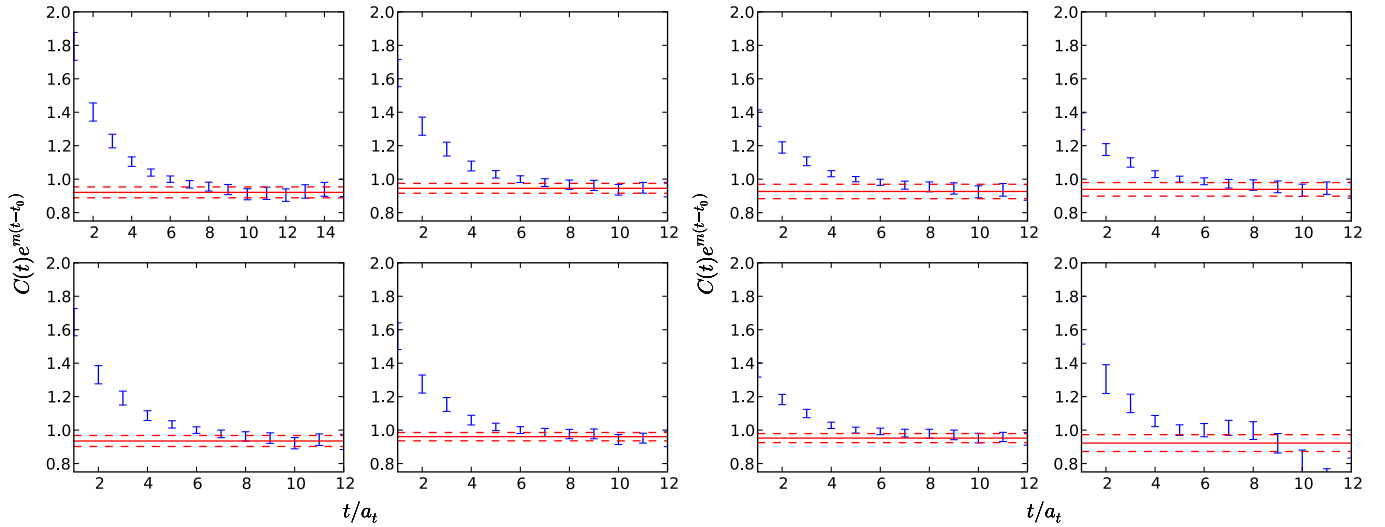
FIG. 11 (color online).　Plots of Eq. (49) versus time for H_g states (left panels) and H_u states (right panels) for $m_\pi = 578$ MeV.

degenerate states (within errors) in the G_{2u}, H_u, and G_{1u} irreps, a pattern with two possible interpretations. It could be a single spin $\frac{7}{2}^-$ state or an accidental degeneracy of a spin $\frac{5}{2}^-$ state and a spin $\frac{1}{2}^-$ state. For $N_f = 2$ QCD and $m_\pi = 416$ and 578 MeV, we see clear evidence for a $\frac{5}{2}^-$ state.

As the pion mass decreases, it becomes increasingly likely that some of the energy levels determined in our simulations will correspond to multihadron states. Disentangling these states from the hadron spectrum will be challenging and will require the use of specially designed multihadron operators. In this paper, as a first step toward the identification of scattering states, we estimate multihadron threshold energies in each of the irreducible representations of O_h. Some of the threshold energies correspond to states with two hadrons at rest. However,

scattering states of hadrons with back to back momenta must also be considered.

On the lattice, a hadron with momentum $\vec{p}$ transforms irreducibly under the space group, which is the semidirect product of the group of three-dimensional lattice translations with O_h. In addition to the momentum vector $\vec{p}$, irreducible representations of the lattice space group are characterized by a label denoting the irreducible representations of the group of lattice rotations which leaves $\vec{p}$ invariant (the little group of $\vec{p}$). For particles at rest, the little group is O_h. More generally, the little group is a subgroup of O_h which depends on the orientation of $\vec{p}$ with respect to the lattice axes. The minimum nonzero momenta on a periodic lattice, of magnitude $2\pi/(N_s a_s)$, are directed along the lattice axes. The little group for such momenta is $C_{4\nu}$.
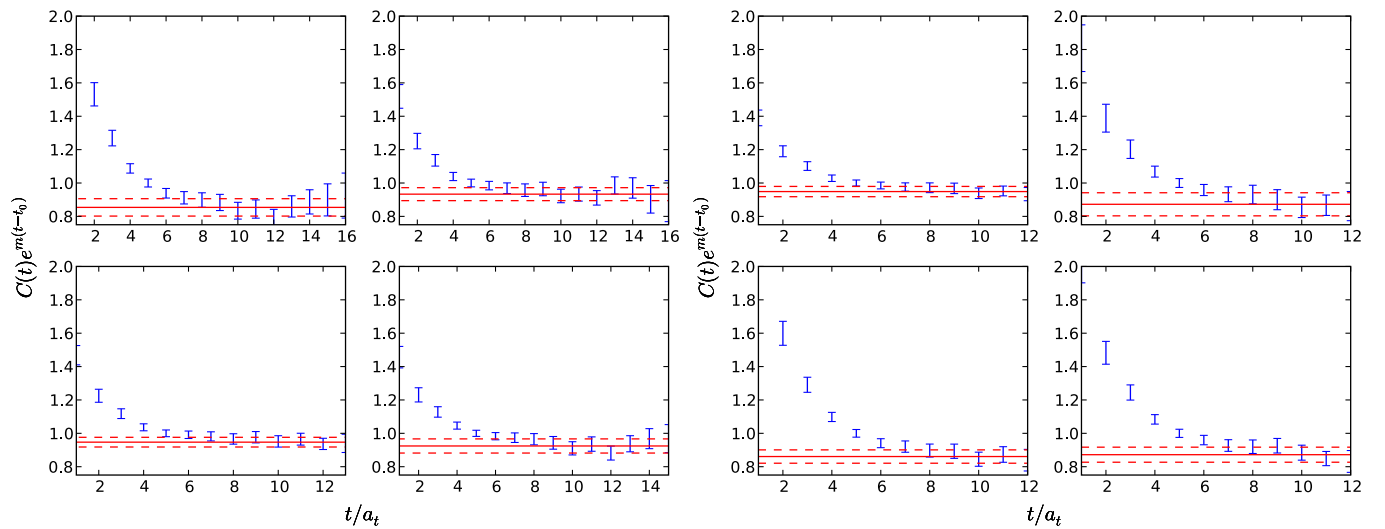

FIG. 12 (color online).　Plots of Eq. (49) versus time for G_{2g} states (left panels) and G_{2u} states (right panels) for $m_\pi = 578$ MeV.

Given the spectrum of hadrons at rest, one can deduce the allowed free-particle energies in any irreducible representation of the space group. To see this, we first note that representations of a lattice little group can be subduced from the irreducible representations of O_h. The subduced representations are in general reducible and may be decomposed into a direct sum of irreducible little group representations. Irreducible representations of the full space group are induced from the irreducible representations of the lattice little groups. Thus, one can relate the irreducible representations of the space group to the representations of O_h. Neglecting cutoff effects, the energy of a noninteracting hadron with momentum $\vec{p}$ is given by $E = \sqrt{M_h^2 + |\vec{p}|^2}$, where M_h is the rest mass of the hadron. Therefore, provided that the hadron rest masses are known, the free-particle energies in representations with nonzero $\vec{p}$ can be determined.

Reference [41] gives the decomposition of direct products of irreducible representations of the space group, including representations with nonzero momentum, into the irreducible representations of O_h. We use this information to identify the allowed multihadron states in each representation of O_h. The energies of multihadron states are approximated by the sum of the energies of their constituents. The empty boxes in Fig. 6 show candidates for multihadron thresholds for both pion masses. Note that $I = \frac{3}{2}$ baryons, which are not considered in this study, can also combine with isovector mesons to form $I = \frac{1}{2}$ two-particle states. However, such states are expected to lie above the thresholds presented here. In both figures, the threshold energies in the G_{1u} and G_{2g} representations correspond to meson-baryon states involving a pion at rest, while the other thresholds involve particles with nonzero momentum. The threshold energies in the G_{1g}, H_g, and H_u representations are degenerate. Our results illustrate the need for a proper analysis of multihadron contamination. Even at the heavier pion mass, many of the measured energy levels lie above the threshold for scattering states. Because of lattice artifacts, finite volume effects, and the interaction between hadrons, the measured multihadron energies are expected to deviate from our estimates. This might explain some of the discrepancies between the predicted multihadron energies and the measured spectrum. However, it is also likely that the interpolating operators used in our simulations, selected on the basis of a quenched study, couple only weakly to the lowest lying multihadron states. Nevertheless, our analysis indicates that multihadron states cannot be discounted, even at the moderate pion masses used in this study.

VII. CONCLUSION AND OUTLOOK

In this work, anisotropic lattices with $a_t = \frac{1}{3} a_s$ are developed for $N_f = 2$ QCD with two pion masses: $m_\pi = 416$ MeV and 578 MeV. The lattice setup and the algo-

rithms used to generate gauge configurations are described in detail. Conventional two-point correlation functions are used to calculate the spectrum of mesons in order to determine the pion masses and to tune the fermion anisotropy to $\xi = 3$, which matches that of the gauge fields. The lattice scales $a_s \approx 0.113$ fm and 0.108 fm are set using the Sommer parameter.

This work builds upon several years of work to develop large numbers of baryon operators, to project them to the relevant irreducible representations of the octahedral group, to optimize the smearing of both the quark and gluon fields in the operators in order to be able to extract clean signals for effective masses, and to prune the operators to manageable sets of 16 operators that yield good signals for baryons. Using the final operators, 16×16 matrices of correlation functions are calculated in each irrep and a variational analysis of the isospin $\frac{1}{2}$ spectrum is carried out. The lowest four energy levels in each irrep are reported. The analysis of the negative-parity spectrum shows a cluster of states near 1.5 to 1.7 times the nucleon mass that includes a $\frac{5}{2}^-$ state, two $\frac{1}{2}^-$ states at somewhat lower energies, and two $\frac{3}{2}^-$ states. This pattern is in accord with the pattern of physical states, although the latter is at a lower overall energy scale. The clear signal for a $\frac{5}{2}^-$ state has not been realized previously. The analysis of the positive-parity spectrum for both pion masses shows that excited states typically have energies about 1.8 or more times the mass of the nucleon state. The question remains open whether as the pion mass is reduced the first excited G_{1g} state will come down to about 1.53 times the nucleon mass, where it would agree with the Roper resonance.

All the excited states in the lattice spectrum are near or above the threshold for πN scattering states. In order to deal properly with that aspect, multihadron operators and all-to-all propagators will be needed. This is an immediate challenge for progress on the $2 + 1$-flavor dynamical lattices [29,42] and it will be addressed in the near future.

ACKNOWLEDGMENTS

[1] T. S. H. Lee and L. C. Smith, J. Phys. G **34**, S83 (2007).

[2] A. Matsuyama, T. Sato, and T. S. H. Lee, Phys. Rep. **439**, 193 (2007).

[3] S. Basak *et al.*, Phys. Rev. D **72**, 094506 (2005).

[4] S. Basak *et al.* [Lattice Hadron Physics Collaboration (LHPC)], Phys. Rev. D **72**, 074501 (2005).

[5] S. Basak *et al.*, Proc. Sci., LAT2005 (2006) 076 [hep-lat/0509179].

[6] S. Basak *et al.*, Phys. Rev. D **76**, 074504 (2007).

[7] S. Sasaki, T. Blum, and S. Ohta, Phys. Rev. D **65**, 074503 (2002).

[8] D. Guadagnoli, M. Papinutto, and S. Simula, Phys. Lett. B **604**, 74 (2004).

[9] D. B. Leinweber, W. Melnitchouk, D. G. Richards, A. G. Williams, and J. M. Zanotti, Lect. Notes Phys. **663**, 71 (2005).

[10] K. Sasaki, S. Sasaki, and T. Hatsuda, Phys. Lett. B **623**, 208 (2005).

[11] K. Sasaki and S. Sasaki, Phys. Rev. D **72**, 034502 (2005).

[12] T. Burch *et al.*, Phys. Rev. D **74**, 014504 (2006).

[13] N. Mathur *et al.*, Phys. Lett. B **605**, 137 (2005).

[14] P. Chen, Phys. Rev. D **64**, 034509 (2001).

[15] M. Okamoto *et al.* (CP-PACS Collaboration), Phys. Rev. D **65**, 094508 (2002).

[16] C. J. Morningstar and M. J. Peardon, Phys. Rev. D **60**, 034509 (1999).

[17] A. C. Lichtl, arXiv:hep-lat/0609019.

[18] K. J. Juge *et al.*, arXiv:hep-lat/0601029.

[19] S. Basak *et al.*, arXiv:hep-lat/0609052.

[20] J. J. Dudek, R. G. Edwards, N. Mathur, and D. G. Richards, Phys. Rev. D **77**, 034501 (2008).

[21] T. Umeda *et al.* (CP-PACS Collaboration), Phys. Rev. D **68**, 034503 (2003).

[22] R. Morrin, A. O. Cais, M. Peardon, S. M. Ryan, and J.-I. Skullerud, Phys. Rev. D **74**, 014505 (2006).

[23] R. G. Edwards and B. Joo (SciDAC Collaboration), Nucl. Phys. B, Proc. Suppl. **140**, 832 (2005).

[24] T. R. Klassen, Nucl. Phys. B, Proc. Suppl. **73**, 918 (1999).

[25] K. Symanzik, Nucl. Phys. **B226**, 187 (1983).

[26] K. Symanzik, Nucl. Phys. **B226**, 205 (1983).

[27] T. R. Klassen, Nucl. Phys. **B533**, 557 (1998).

[28] M. Luscher, S. Sint, R. Sommer, P. Weisz, and U. Wolff, Nucl. Phys. **B491**, 323 (1997).

[29] R. G. Edwards, B. Joo, and H.-W. Lin, Phys. Rev. D **78**, 054501 (2008).

[30] S. Duane, A. D. Kennedy, B. J. Pendleton, and D. Roweth, Phys. Lett. B **195**, 216 (1987).

[31] M. Hasenbusch and K. Jansen, Nucl. Phys. **B659**, 299 (2003).

[32] J. C. Sexton and D. H. Weingarten, Nucl. Phys. **B380**, 665 (1992).

[33] R. C. Brower, T. Ivanenko, A. R. Levi, and K. N. Orginos, Nucl. Phys. **B484**, 353 (1997).

[34] I. M. Omelyan, I. P. Mryglod, and R. Folk, Comput. Phys. Commun. **151**, 272 (2003).

[35] T. Takaishi and P. de Forcrand, Phys. Rev. E **73**, 036706 (2006).

[36] D. H. Weingarten and D. N. Petcher, Phys. Lett. **99B**, 333 (1981).

[37] C. Aubin *et al.*, Phys. Rev. D **70**, 094505 (2004).

[38] C. Bernard *et al.* (MILC Collaboration), Proc. Sci. LAT2006 (2006) 163 [hep-lat/0609053].

[39] C. Morningstar and M. J. Peardon, Phys. Rev. D **69**, 054501 (2004).

[40] B. Blossier, G. von Hippel, T. Mendes, R. Sommer, and M. Della Morte, Proc. Sci. LATTICE2008 (2008) 135.

[41] D. C. Moore and G. T. Fleming, Phys. Rev. D **74**, 054504 (2006).

[42] H.-W. Lin *et al.*, Phys. Rev. D **79**, 034502 (2009).